Modeling Applications for Informed Self-Powered System Design

---

A

Thesis

Presented to

the faculty of the School of Engineering and Applied Science

University of Virginia

---

in partial fulfillment

of the requirements for the degree

Master of Science

by

Katheryn Flynn

May 2023

APPROVAL SHEET

This

Thesis

is submitted in partial fulfillment of the requirements
for the degree of

Master of Science

Author: Katheryn Flynn

This Thesis has been read and approved by the examing committee:

Advisor: Benton Calhoun

Advisor:

Committee Member: Bradford Campbell

Committee Member: Scott Barker

Committee Member:

Committee Member:

Committee Member:

Committee Member:

Accepted for the School of Engineering and Applied Science:

Jennifer L. West, School of Engineering and Applied Science

May 2023

Abstract

The Internet-of-Things (IoT) has the potential to revolutionize our understanding and real-time awareness about the world around us, to make our lives simpler, safer, and healthier. However, the growth of the IoT depends greatly on how efficient and cost effective the technology is. Many battery-based systems suffer from their restricted power supply lifetime, which cause regular maintenance, replacement, and downtime costs. Energy-harvesting systems can suffer from poor dependability when environmental sources supply insufficient power for their operation, which leads to poor application quality. In general, when the system's power consumption is lowered, both the lifetime and the dependability are increased. Therefore, to support the ever growing scale of IoT device deployment, dominating factors of system power consumption must be addressed.

The goal of this work is to highlight some capabilities of modeling with respect to self-powered systems, and to illustrate the need for modeling to be further developed to aid in system design. The scale and impact of IoT devices are largely limited by the lifetime or longevity of the systems in their respective environments. From a systems perspective, modeling can aid in the realization of the design space that restricts a designer's boundaries by addressing individual components' contributions to overall system power. Further, test modes and models can be paired with statistical representations of environments to determine the functionality of a system when it is being supported solely by the environment. This is useful to help maximize the reliability and availability of deployed sensor nodes. From a sensing perspective, this work calls attention to the impact of physiology in on-body sensing. A three-part model is presented to encapsulate the impact of human-electronic interaction on ULP sensing and its accuracy. Modeling is an extremely powerful tool to aid designers in the exploration of the boundaries of current technology. When customized to specific applications, models can lend powerful insight to the design knobs that can and need to be explored for optimal solutions.

List of Figures

Contents

1. Fundamentals of Self-Powered Systems

To create a model to provide insight into the relationship between power consuming devices, and the energy for which they consume from the environment, fundamentals of these devices must be defined. **Energy** is a property of matter, which allows it to perform work. **Energy harvesting** is the process of collecting and storing small amounts of energy from ambient sources, such as light, or heat, which can then be used to do work. In the context of electrical sensor nodes, work is the performance of an operation. An operation for a sensor typically includes the conversion of a physical quantity into an electrical signal, typically done with a transducer, that can then be used to make a calculation, and be further transmitted. When a sensor performs an operation, it consumes energy. Power is the rate at which energy is used, transferred, or generated. Power usage in sensor nodes can be continuous or intermittent. In the continuous state, power is consumed at a constant rate and therefore energy is directly proportional to time. If the system is intermittent, power is consumed in bursts, and the total energy is found by the duration of the burst. Energy harvesting sensors known as self-powered systems (SPS) use energy from the local environment to fuel the operations that they perform. This energy is either directly consumed for operations, or stored by the device to later be utilized.

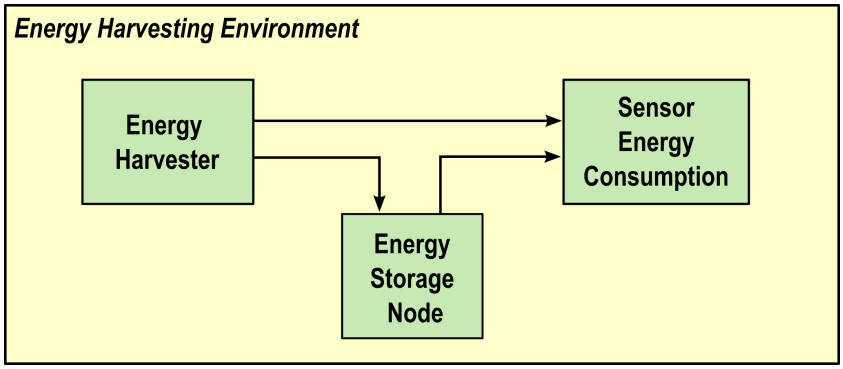

Figure 1: *The flow of energy in a Energy Harvesting system*

The sensor that performs operations can exist in two fundamental states, 1. Available, in which the environment can provide sufficient energy for the system to operate as desired, and 2.

Unavailable, in which there is not enough energy to perform an operation. In a typical battery-powered sensor, the lifetime of the device is synonymous with the runtime, or the amount of time remaining for a device to perform operations until the device has no further energy to expend. In general, these sensing nodes will operate from some stored and finite quantity of energy E_{store}, and if we temporarily take a simplified approach to assume that the node will consume energy at a constant rate P_{node}, then the lifetime of the node will follow the relationship

$$\text{Lifetime} \propto \frac{E_{store}}{P_{node}} \tag{1}$$

Naturally, using a larger battery to provide more E_{store} or making the node more energy-efficient to decrease P_{node} will increase the lifetime of the overall system. Energy harvesting is an increasingly popular method to effectively increase E_{store} by harvesting freely-available ambient energy to supplement the original finite amount of stored energy. In an energy harvesting system, the lifetime of the device is effectively limitless as long as it continues to properly harvest energy and perform operations. The runtime is the same as in a battery supplied system, the time until an available sensor becomes unavailable. However, with an energy harvesting system, the device has the opportunity to repair, or recharge.

Perpetual operation for a self-powered system requires that the following inequality be satisfied which dictates the relationships between harvesting and consumption of energy over time. The variables P_H and P_L are the instantaneous harvesting and effective load powers. It is assumed that any DC-DC efficiency losses are lumped into P_L. The harvesting efficiency factor, $\eta(x)$, is a function of numerous variables from the harvesting circuit which will consume some amount of quiescent current, which is a design concern to maximize the harvested power, P_H.

$$\eta(x)P_H(t) - P_L(t) > 0 \tag{2}$$

In this representation, it is important to understand that no energy storage devices have been deployed, and that in order to satisfy the requirement, the load must consume less than what is

available in the environment after the harvesting efficiency hit. The harvested power can also be used to recharge a battery, however the nature of batteries to store energy chemically leads to decreased cycle life (endurance) that causes their maximum capacity to deteriorate the more times that it is charged and discharged. Batteries also suffer from self-discharge that would cause a fully-charged battery to eventually lose its stored energy over an extended period of time, even if no load is attached. Super-capacitors offer a more robust means for storing energy that behave more ideally over time and are therefore a common energy storage mechanism for long-lifetime IoT nodes. If an energy storage device is utilized, the system can consume the capacity of the stored energy beyond what the environment could instantaneously provide, given that the storage node is fully charged. The following inequality introduces the effects of the storage node.

$$E_{T2} = \int_{T1}^{T2} \left[\left[\eta(x) P_H(t) \right]^+ - P_L(t) \right] dt \; - \int_{T1}^{T2} P_{E,leakage}(t) dt \; + E_{T1} > \; 0 \tag{3}$$

$E_{T1}$is the initial energy stored at the beginning of the time period, and the upper bound of the storage device is given by (4).

$$[x]^+ = \begin{cases} 0, E(t) \geq E_{max} \\ x, E(t) < E_{max} \end{cases} \tag{4}$$

Similar to the system without a storage device, the integral on the left represents the amount of energy that is effectively harvested, or consumed over time. If the storage device reaches capacity, the system will not be able to harvest until it drops below the threshold. The integral on the right represents the inevitable leakage that all energy storage devices experience. If the system can satisfy the above equation continuously over a period of time, then it may be deemed energy neutral, or energy positive. Energy neutral describes a system where the inequality is satisfied and $E_{T1} = E_{T2}$, which means that the system does not die, and its final energy state is the same as its initial energy state or there is no net energy gain/loss. An energy positive system is where the inequality is satisfied and $E_{T1} < E_{T2}$. An energy negative system

must fail $E_{T1} \leq E_{T2}$. A SPS will not always belong to one type. Depending on the period of time, a SPS may be neutral, positive, or negative. However, in generality, the goal for a SPS is to remain energy neutral and positive as much as possible. Self-powered system failure due to lack of energy is related to either or both; poor harvesting conditions, and excess power consumption by the system. If these happen regularly, then the self-powered system can't perform its desired function, and might not be a worthwhile application. Figure 2 illustrates the changing states of a SPS with respect to the energy that is available to be consumed. When the available energy drops below the minimum operational energy, the system fails and remains in this failure state until there is enough energy for start-up.

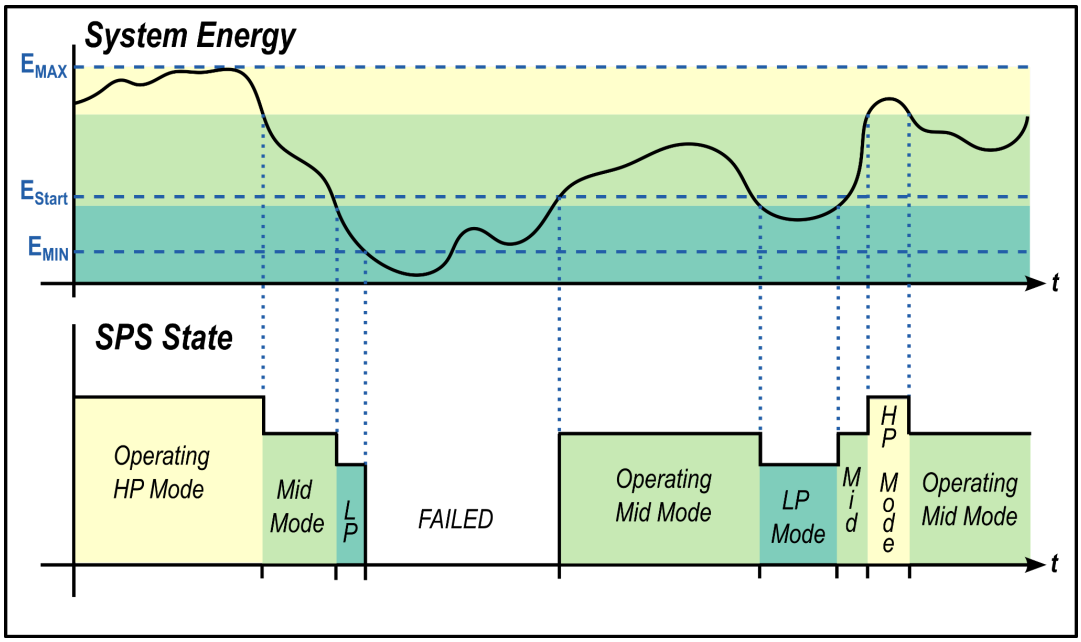

Figure 2: *Example of a time-domain energy trace for a SPS and the subsequent operational modes(LowPower, MidPower, and HighPower) based on the available energy for consumption*

The reliability of a SPS, or the degree to which the SPS can perform operations, is dependent on the environment that it is harvesting from, and the power consuming characteristics of the system, or the load. If a SPS is considered as a repairable system, or a system that is designed to be returned to its original state following "breaking-down", the

reliability is simply probability that the system will perform its desired operation over time. In a repairable system, a common metric is mean-time-between-failure (MTBF), which denotes how quickly the system will fail after a start-up. MTBF is calculated by taking the difference in time between each system failure, and the previous recovery and dividing it by the number of failures.

$$MTBF = \frac{\sum_{n=1}^{N} (\tau_{F_n} - \tau_{R_{n-1}})}{N} \quad (5)$$

Conversely, maintainability describes how easy it is for a system to repair. In SPS, this is the time that it takes to harvest the energy required for operation, defined by mean-time-to-repair (MTTR). MTTR calculates the time difference with failure states.

$$MTTR = \frac{\sum_{n=1}^{N} (\tau_{R_n} - \tau_{T_n})}{N} \quad (6)$$

A modulating environmental supply will cause a change in the load's ability to carry out operations; and a variable operation will change the energy demand from the environment. Reliability and maintainability combine to a third SPS metric, availability, which refers to the system's capability to be used without constraint in time, or the probability that a system will be able to fully operate at a given point in time. Availability is found by combining reliability and maintainability to quantify the percentage of time that the system will be accessible.

$$Availability = \frac{MTBF}{MTBF + MTTR} \quad (7)$$

Together, reliability, maintainability and availability can quantify the success a specific SPS will have when deployed in a specific environment. To help realize reliability and availability, a virtual prototyping framework for modeling systems composed of power consuming components will be paired with statistical models for environments generated from sampled data sets.

2. Background

In the past there have been modeling efforts to optimize energy harvesting system methods for self-powered systems, but none that encapsulate whole system tradeoffs as well as

environmental variability. Dondi et al. presents a method for optimizing a solar harvester with maximum power point tracking for SPS by focusing on maximizing the harvester's efficiency in the transfer of energy from solar panel to energy storage device. In this case, a detailed model of just the photovoltaic panel and the harvester is used to understand the interaction between these components through simulation. This model is valuable to encapsulate the efficiency losses that occur in these specific components but it does not provide any insight into how the efficiency impacts the performance of the SPS. Castalia is a discrete event simulator built on OMNeT++ which uses unit models to represent the connection of sensor nodes over a common wireless channel model [2]. This tool is particularly useful in creating a testbed for distributed algorithms or protocols in dynamic changing wireless channels. Again, the tool lacks the capability to understand the impacts of design changes within the components of these unit models on the performance of the overall system, and further, it has no ability to connect the system to any sort of dynamic energy source as different environments provide. GreenCastalia is an extension of the Castalia simulator which provides an energy harvesting simulation framework [3]. It allows designers to simulate networks of unit models with heterogeneous harvesting capabilities by defining energy harvesters, energy storage devices, and energy management algorithms. However, both Castalia and GreenCastalia can only report on network-related system characteristics, and not component-level considerations. Other modeling simulators also provide network level tools such as Contiki and TinyOS, which emulate networks of communicating nodes [4,5]. Again, representations of hardware power consuming characteristics are lacking and there is no capability of enabling a SPS model.

Outside of hardware modeling, data collection and modeling of the environment is a large task that requires ample time to fully characterize. A few efforts have been made in this area of research, including the characterization of indoor office environments through long-term indoor radiant energy measurements [6]. In this study, the transient indoor radiant light energy is used to generate algorithms for optimizing energy consumption based on the predictability of the environment. The limit of this work in informed SPS design, is the interaction between the energy consuming device and the energy supply. The optimization of consumption is also

dependent on the state of the system which is typically dynamic. Thermo-electric energy harvesting is also a widely explored area due to the demand for on-body wearable medical sensing devices. A comprehensive model for thermoelectric body heat was developed using measurements of a TEG during a variety of physical activities [7]. This work takes into account the metabolic processes of the body as well as the body's interaction with the environment during activity.

Each of these modeling efforts have provided insight into specific areas that contribute to the design of self-powered systems. But in each case, there is a missing link between circuit and hardware definition and simulation in real life environments. The resulting design tool research gap for effective deployment and analysis of devices dynamically consuming energy from the environment is the focus of this work.

3. Modeling Self-Powered Systems

3.1 Load Modeling

Deployable self-powered systems have the potential to revolutionize our real-time awareness of the world around us, provided the cost of deployment and maintenance does not outweigh the sensing benefits. This cost-analysis of SPS deployment is largely application specific, given different use cases for different sensing modalities. However, a generalized modeling tool that can provide a user, or prospective user, with the capability to analyze the overall quality and performance of their specific application, enables design decisions to optimize system efficacy. There are a few major facets of a self-powered system. The first is the system itself, or the energy consuming components that carry out the operations of data collection. In order to define the characteristics of a system as a whole, the model allows the user to build up a hierarchy of power consuming components that define the system as a whole [8]. There are three major element types that are used to define the hierarchy, Components, ComponentGroups, and VoltageRegulators, as shown in *Figure 3*.

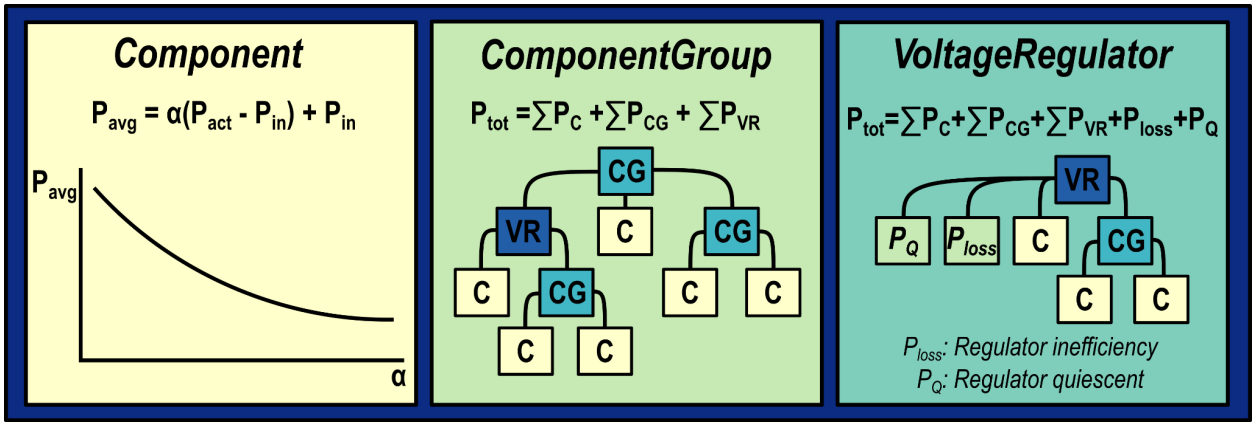

Figure 3: *The three major component-like elements used to model the connection of power consuming devices in a self-powered system.*

A Component is the only leaf node, when the system is considered as a tree structure, which provides the user with the most atomic level of power consumption modeling. This class assuming a universal duty cycle type model for power consumption of every object, represented by:

$$P_C = f_c(v_1, v_2, \dots) \approx \alpha_C (P_{active,C} - P_{in-active,C}) + P_{in-active,C} \quad (8)$$

where v_i represents user defined variables that impact a particular components power consumption, P_C. This modeling method allows the designer to see the impact of changing variables, to their own degree of granularity, depending on the complexity of the models they employed. Once all of the Components have been modeled, the designer can specify how they link together through ComponentGroups. ComponentGroups allow for an arbitrary number of component-like objects to exist “beneath them” in order to abstract sections of the system away and to check for consistency in operation voltage for connected devices. A tool in the model recursively traverses through the hierarchy to sum the total power, or current, of the particular ComponentGroup. The total power for a specific ComponentGroup is given by the sum of all the component-like objects that fall under that specific ComponentGroup, as illustrated in *Figure 3.* The VoltageRegulator is similar to the ComponentGroup class in that it groups component-like

objects that exist under it, but it also takes into account specific aspects of supply regulation. The VoltageRegulator accounts for inefficiencies in supply regulation as well as the static power consumption as a result of the regulator circuit. Efficiency and regulator power are parameters which can be controlled by custom user models, or look up tables. *Figure 3* illustrates the summation of power for a particular regulator, including the power loss due to regulation inefficiency and the quiescent power consumption of the regulator itself. In general to use this modeling framework, a designer would start with defining the leaf-components, and work their way back up the tree grouping components with ComponentGroups and Regulators, until they have successfully created one top level ComponentGroup that all other branches stem from.

3.2 Load Tools

Once a system has been defined, various modeling tools can be used to evaluate the constraints of its operating space. By building the system in a hierarchical fashion, complex systems can be plotted in a ‘sunburst’ plot which graphically displays the weight of each block's power consumption with respect to the tree structure. An example of this is shown in *Figure 4,* where you can identify the component groups via the color they are grouped with, corresponding to a specific regulator. This visual is useful to a designer to determine which block should be targeted most highly for power reduction when aiming for ultra low power designs. As is obvious with the visual, in this example system, it would be most advantageous to reduce the power of the BLE RX because that is currently the highest percentage consumer in the system, which leads to the next tool of duty cycle visualization. However, by defining the duty-cycling characteristics of each block we can plot their power consumption across duty cycle and the total system power to determine the overall impact, as shown in *Figure 5.* Many times, this method of characterization of the whole system by “sum of parts” makes sense, and can fully define the operation of the system. In other cases, individual components will have different operation points with respect to each other, which requires another modeling tool enabled by the definition of operational modes. The Mode class is used to group components at varying operation points to be evaluated. *Figure 2* illustrates a system that has 3 discrete modes; HP,

Mid-Power, and LP, where each of these modes is composed of the same components but at different combinations of operating points to achieve different degrees of system performance. Once modes are defined, further abstraction can be gained by defining a system operation, which is a sequence of modes that the system will move through in a period of time. Operations are base units of performance for a SPS which are used to evaluate the performance of a system when deployed in an environment. A user might define a few operations for a given system to evaluate what degree of performance, by the number of operations that can be performed by a system as an environment changes. Other metrics such as the minimum, maximum, and average system power can also be used to consider the reliability of the deployment.

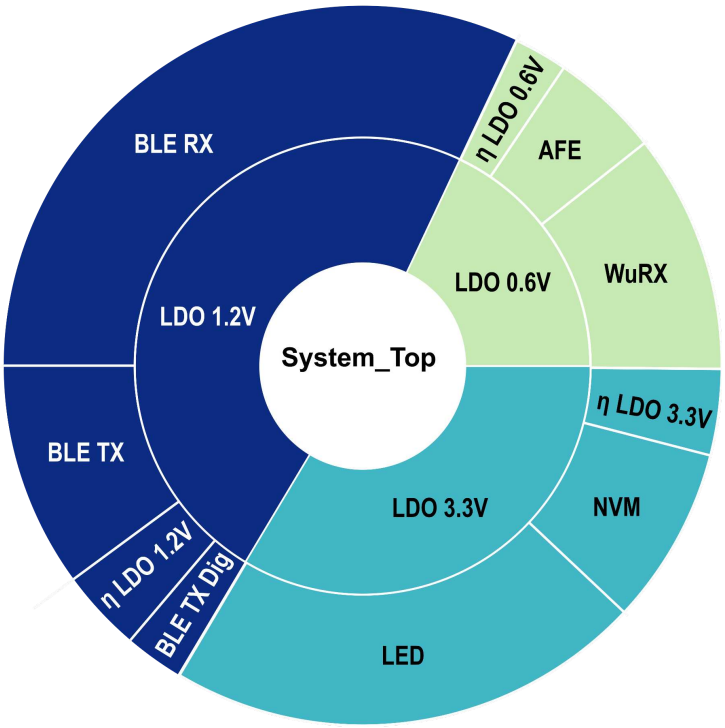

Figure 4: *Sunburst plot of a system hierarchy weighted at each layer relative to power consumption.*

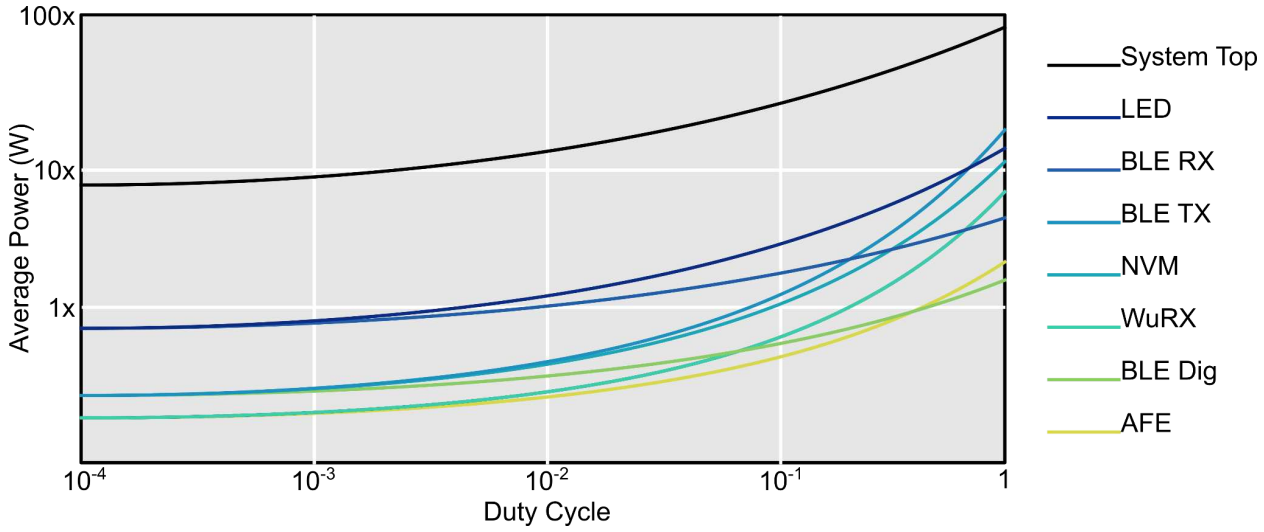

Figure 5: *System Power consumption with the duty-cycling of components*

3.3 Environmental Characterization

To evaluate the performance of a SPS, it is necessary to define the environment's energy availability characteristics that will supply the power to drive operations.Tiny battery-less nodes deployed in different settings will experience relatively unpredictable energy availability. The aim of implementing modeling tools is to quantify statistical characteristics, as well as analytical models of environments to allow for informed design of self powered systems. One of the greatest challenges with this goal is the lack of available information regarding energy in environments. In order to fully realize these characteristics, months or even years of continuous data collection, in different domains, in specific environments, is necessary. For the purposes of this analysis, we will evaluate two environments that are of general interest to deployable self powered systems. The first of which is the energy available from lights in a conference room, and the second is available heat energy from the human body's thermoregulation. These two mediums are particularly interesting because of their prospects for future device deployment, the monitoring of air quality, room occupancy, and usage are of interest in conference rooms, and medical wearables are driving interest in on-body sensing.

A 2011 study at Columbia University aimed to characterize the energy availability of indoor environments by conducting a 16-month long indoor radiant energy measurement

campaign, resulting in a data set of energy measurements that will be used in the following discussion [6]. The dataset provides irradiance (I), or the radiant energy incident onto a surface in W/cm^2. The first step in characterizing these measurements for the purpose of powering deployable systems is to determine the quantity of energy available to the circuit from the irradiance. Irradiation (H_T) in J/cm^2 is the integral of irradiance over a specific time period, T. Generally for light energy, we will recognize a diurnal profile when T = 24 hours, and denote this daily irradiation as H_D. The amount of energy that a device has access to, D, is dependent on the characteristics of its PV cell. For a cell of area A and efficiency η, D = AηH. A schematic of these energy relationships is found in *Figure 6*, where a capacitor is introduced as energy storage, with capacity C. The energy that is able to be harvested by the PV cell can be stored and used by the main device, or used directly by the main device depending on the needs of the system at the time.

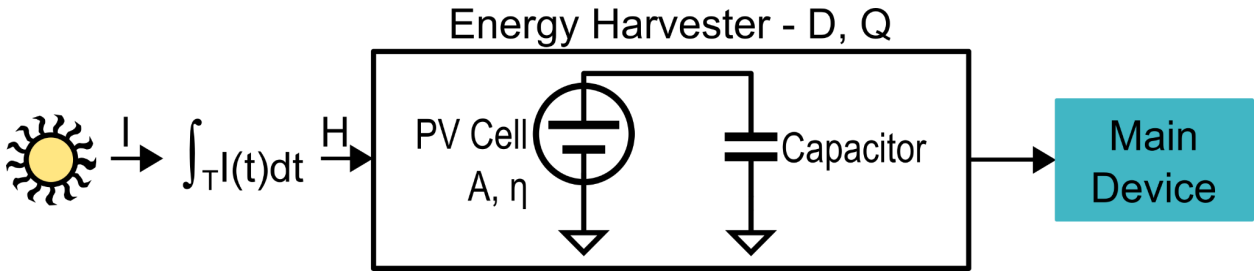

Figure 6: *The relationships between irradiance (I), irradiation (H), energy available to a device (D), and energy collected in storage (Q).*

Figure 7 shows the measured values of daily energy (E_d) in two different locations over 15 days, as you can see, there are significant differences at different locations: on average in Office A, 2.9 J/cm^2/day is received by the testing boards, Office B receives only 1.1 J/cm^2/day. The difference likely stems from different office locations and layouts, and even occupant behavior such as raising and lowering the blinds. It should also be noted that there is a significant difference day to day at the same testing site. Office A's standard deviation is 0.8 and Office B's is 0.56. In addition to temporal differences between days, there may be significant variation within a day itself, with the quantity of variation dependent on the location as shown by the right

side plot in *Figure 7.* The shapes of the curves in this plot are quite different. We can extrapolate that it is likely in Office C, that the testing board gets the most energy from sunlight, as we can observe diurnal variations. Office D suggests that the source of energy is more artificial in nature because of the flatness in the curve during most of the working day. The diversity in energy availability across similar but varying locations leads to a necessity for modeling environments through statistical models that can be varied based on the specific deployment application that the designer has in mind.

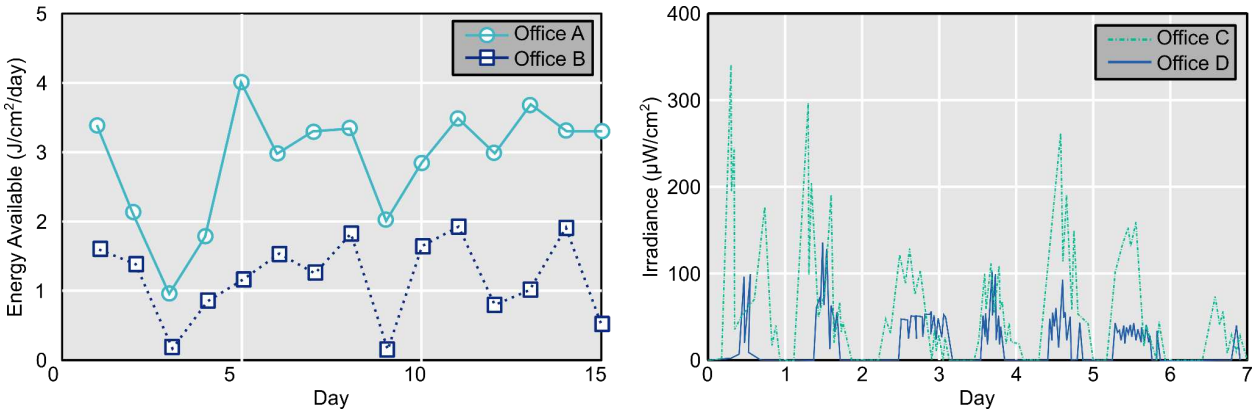

Figure 7: *Indoor energy availability measurements: left; total energy available per day in two different locations over 15 days and right; irradiance in two different locations over 7 days*

A 2020 study at North Carolina State University worked to characterize the energy the thermoelectric generators (TEG) are capable of harvesting from body heat. By taking measurements across a variety of individuals during different levels of activity, they aimed to create a comprehensive model combining an analytical TEG model with biological models for the human body, rather than relying on statistical conclusions from data analysis as suggested in the office space study [7]. The results from this model can be observed in *Figure 8* where the TEG output voltage is measured with a test subject and modeled over time.

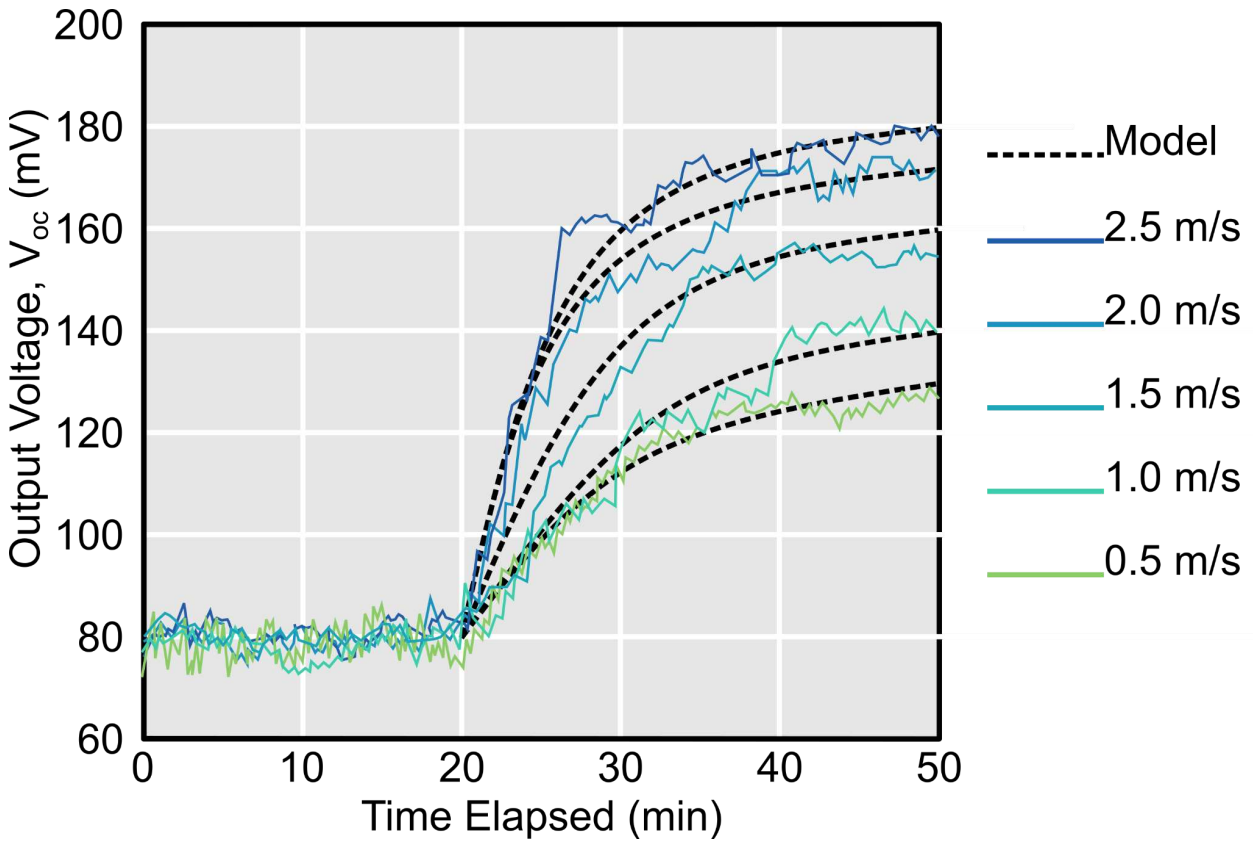

Figure 8: *TEG output voltage measured on a treadmill during walking or running at different speeds, dashed lines correspond to modeled output.*

4. Modeling PPG Sensing

4.1 Background

Wearable health monitoring is a fast growing industry with devices like the Apple Watch, Fitbit, and Oura Smart Ring offering health related data during everyday life. Previously, acquiring these metrics would require much larger, inconvenient systems that aren't available outside of hospitals and other facilities. Wearables also offer healthy individuals information about their heart rate during exercise and other fitness related metrics that help them optimize their health. Continuous blood oxygen sensing is also crucial in monitoring COVID-19 symptoms such as silent hypoxemia [9], a condition where blood oxygen saturation(SpO_2) drops suddenly, and other conditions such as sleep apnea, chronic obstructive pulmonary disease (COPD), anemia, and lung cancer [10]. PPG has become a standard sensing technique for detecting heart rate

and SpO_2 of the individuals using wearable health systems. PPG sensors use LEDs to illuminate a user's skin and then measure changes in the reflected light that occur due to the presence of varying hemoglobin levels through the cycle of a heartbeat. Signal strength is dependent on the current produced by the photodiode in the PPG sensor which is in turn dependent on the quantity of light reflected by the subject's skin. PPG sensing uses an analog-front end (AFE) and microcontroller (MCU) to interface with the sensor. The level of noise in the AFE must be smaller than the signal in order for the PPG waveform to be usable. This requirement is examined by calculating the signal-to-noise ratio. Due to its optical nature, PPG is heavily dependent on the optical properties of the user's skin but very limited research has been done on the effect of skin type, melanin concentration and BMI on this type of sensing [13,14,15]. Only within the last few years have researchers tried to quantify these effects on the accuracy of PPG signals. In commercial systems, this is addressed by increasing LED current and dynamic range which increases the power consumption. Still, some users with darker skin tones and/or tattoos, referred to in this work as "less reflective", have reported inaccurate heart rate when using these systems. A 2022 cohort study of patients admitted to hospitals with COVID-19 found that, in a clinical setting, PPG based SpO_2 overestimated the actual blood oxygen saturation of Asian, Black and non-black Hispanic patients as compared to white patients. This overestimation led to unrecognized eligibility or delay in administration of COVID-19 therapies[17,18].

4.2 Self-Powered Sensing

Another challenge with popular wearable devices is that they are largely limited by battery power, creating a limited lifetime of use between charge cycles. They may be sufficient for intermittent monitoring on healthy users, but they cannot provide long term and/or continuous monitoring that is required for more critical wearable health applications. A better long-term solution is the implementation of self-powered systems (SPS) for wearable health. Due to the natural thermoregulation of the human body, wearable systems have the potential to be powered by on-body thermo-electric generators (TEG). The available power from these on-body

TEGs (4–21 μW/cm2 at best) is far too low to power current commercial devices [12]. Custom systems-on-chip (SoCs) targeting biomedical applications have been shown to achieve ultra-low power (ULP) consumption (<1 μ W) which indicates they can function as self-powered systems (SPS) [13]. As shown in *Figure 9*, many photoplethysmography (PPG) sensing channels do not operate at a low enough power for self-powered operation. Some of these references have the potential to operate as self-powered systems, but not reliably and only in certain configurations that may affect the quality of a signal output, measured by signal to noise ratio (SNR). It is important to note that none of the cited works discuss the performance across different skin phototypes or the impact of physiological variation [15], [21]–[26], a main focus of this publication. In ULP designs, increasing the LED current is not an effective strategy because this resultant increase in overall system power further limits SPS capability. Therefore, other variables must be adjusted to design an ULP PPG sensor that can operate as a self-powered system and maintain accuracy for skin that reflects less light and those with higher BMIs.

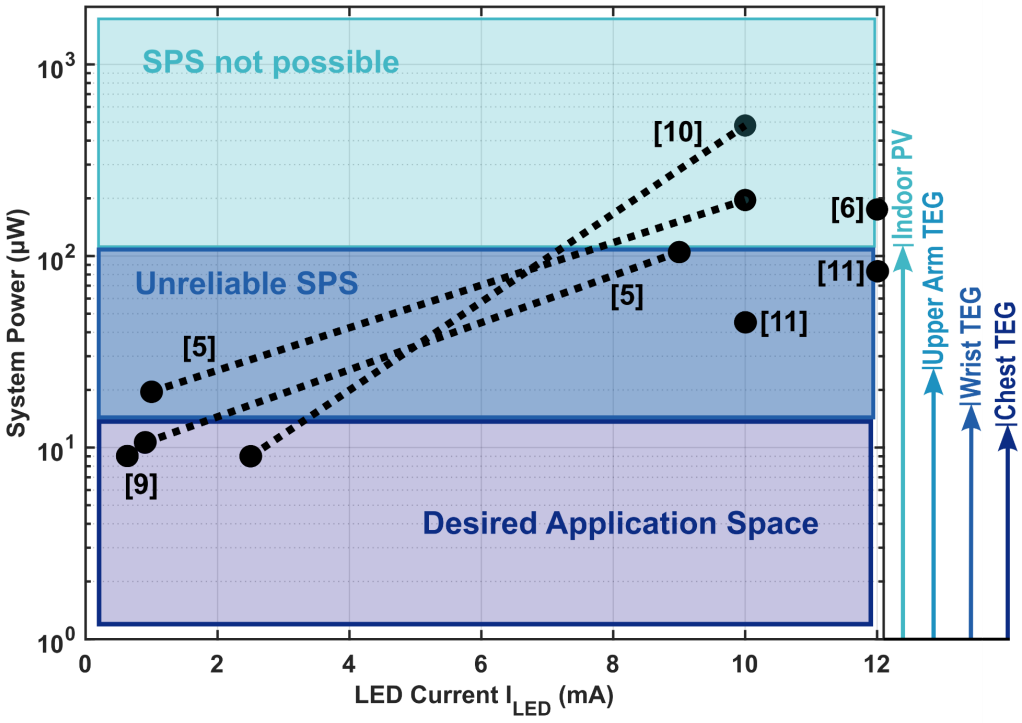

Figure 9: *Power for state of the art PPG systems, which is often higher than what can be supported by on-body TEG or indoor PV.*

This chapter introduces a novel model that uses both physiological data related to skin tone and BMI and circuit metrics to determine the effect of both skin tone and BMI on low-power PPG sensing. Previously, these physiological factors have been examined independently, but an understanding of how their combined effect can reduce the SNR of a PPG signal has not been determined. Understanding the relationship between physiological factors and circuit performance, specifically, quantifying the impact these factors have, through a model allows designers to make decisions without expensive on-body testing. This work utilizes an application-driven model and on-body measured results to show how metrics like LED current, transimpediance amplifier (TIA) gain and sampling frequency can be scaled to reduce the power consumption while still producing a viable PPG signal for all skin phototypes and BMIs. It also compares the model of the custom PPG AFE chip from the RLP-VLSI group at UVA [24]to a commercially available one and compares the results from both to measured results from 23 participants. This work demonstrates the potential for low-power (13μW) PPG sensing at fingertip with an SNR of 65 dB for all skin phototypes using a model based on the custom AFE chip and the SFH7060 PPG sensor from Osram [27]. These results are confirmed through preliminary on-body testing with this same hardware. This supports accurate, personalized PPG sensing that can be powered by on-body TEG harvesting. The trade offs between power and accuracy are examined across a range of skin phototypes and BMI for the purpose of determining which design variables can lower power and achieve accurate operation for all individuals. This work also demonstrates the necessity of examining performance across skin phototype and BMI for inclusive SPS operation. It specifically seeks to show how skin phototype and BMI affect photodiode current (I_{pd}) and, as a result, SNR. It then examines techniques for compensating for this drop in SNR and the resulting power consumption.

4.3 Model Description

A three-part model is used to examine the relationship between PPG sensing accuracy, system power consumption, skin tone and BMI. This model consists of a human skin reflectance

model, a PPG sensor (LED and Photodiode) based on a commercial SFH7060 PPG sensor [26] and an AFE model. The two versions of the AFE model are based on a custom low-power AFE from [16] and the TI AFE4404 [27]. The green, red, or infrared emitter of the PPG sensor illuminates the skin of the user drawing current I_{LED} from voltage supply V_{LED}. This light is then reflected by the physical composition of the user, with varying quantities dependent on physiological factors, including skin phototype, dermal thickness, dermal blood content and more. The photodiode measures the reflected light, producing ac current i_{ac} which represents the pulse and DC offset current I_{DC}, as illustrated in *Figure 10*.

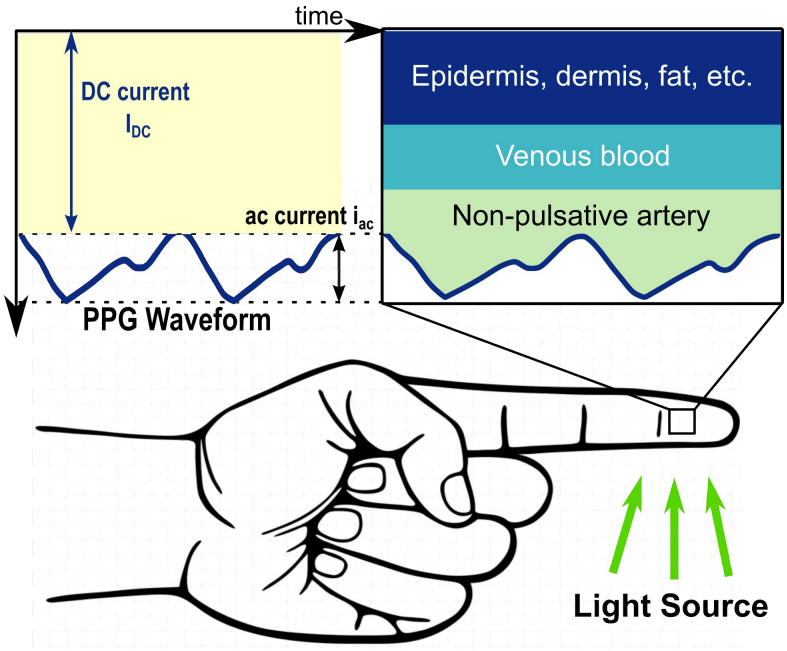

Figure 10: *An overview of the PPG sensing mechanism and the resulting signal in the photodiode, composed of ac and DC current.*

The AFE processes this waveform to produce a voltage which can be used to determine blood oxygen saturation. Two metrics of interest in these AFEs are gain and dynamic range. Dynamic range is the ratio of the highest signal level a system, in this case the AFE, can handle to the lowest signal level it can handle. Gain can be used to maximize the AC component but doing so also increases the DC component. This becomes a problem when the gain is so high that the DC component of a signal saturates the amplifier and an AC signal can not be measured. If the

AC component of a signal is increased by too much, the dynamic range may need to be expanded to accommodate it. The custom AFE reports a dynamic range of 102dB and the TI AFE reports a dynamic range of 100dB. Both the custom and TI AFE have DC offset cancellation (DCOC) capabilities that allows them to reduce the DC component of the signal while maintaining the amplitude and integrity of the AC component. Though different DCOC settings are not explicitly examined in this model, their value is clearly shown and discussed in the results. The goal of this research is to identify strategies that lower the power consumption of PPG sensors while maintaining SNR values that indicate effective sensing across all skin phototypes and BMIs. The three-part model, as shown in *Figure 11,* demonstrates the relationships between skin phototype and BMI and SNR and power in a PPG sensing AFE system and provides bounds for the available design space.

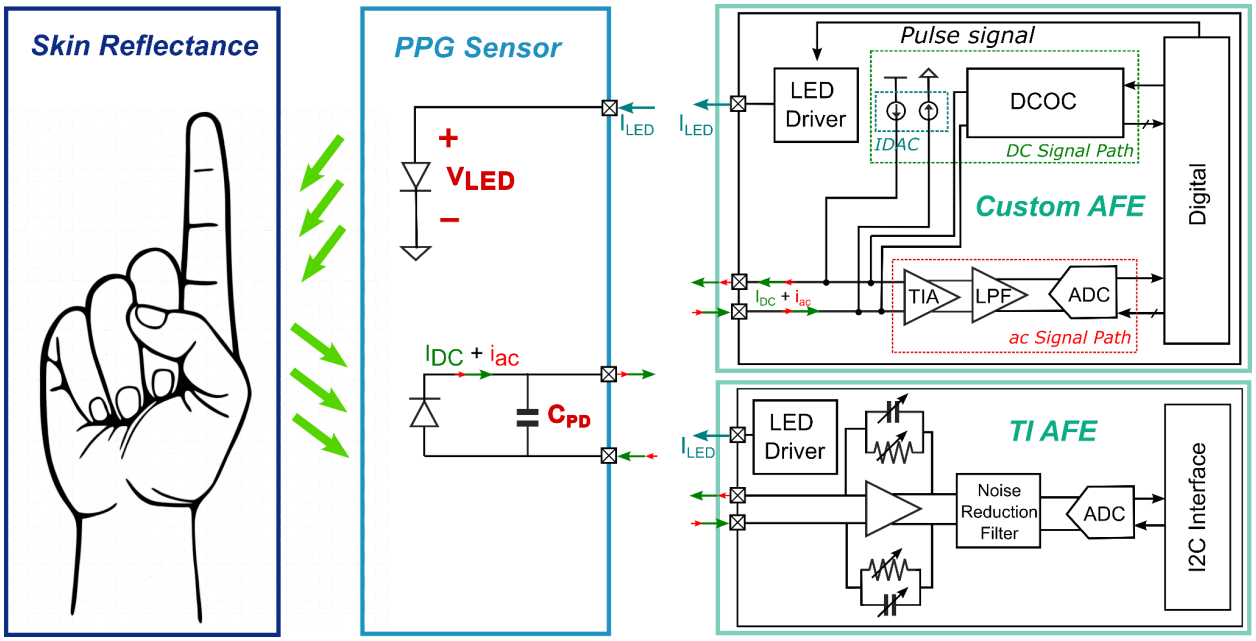

Figure 11*: Three part model structure including skin reflectance model, PPG sensor model, and AFE model. A custom ULP AFE and a COTS TI AFE were both modeled and used interchangeably in order to observe the impact of various design knobs.*

4.3.1 Human Skin Reflectance

The first portion of this work models reflectance of human skin, a major factor in the accuracy of PPG sensing on different skin tones and for people with different BMIs. To start, it is important to understand the physiology behind a PPG signal. As light from the LED enters the skin, it passes through the epidermis and dermis and reaches the artery. The pulsatile nature of blood in the artery causes changes in the light reflected back to the photodiode. In this model, two ways to quantify these effects are used; reflectance, meaning the amount of light reflected by the user's finger, and the AC/DC ratio of the photodiode current. This further simplifies the effect of different physiological factors by focusing on skin tone and BMI. In dermatology and related fields, researchers quantify skin tone and determine melanin concentration using the Fitzpatrick scale [22]. The melanin concentration directly impacts how much light from the LED is reflected back to the photodiode in the PPG sensor. This thesis uses “skin phototype” to discuss the different skin tones and resulting differences in reflectance. It is also important to note that the visible appearance of human skin does not necessarily relate to its reflectance [15]. Factors such as dermal thickness, blood content, radial artery depth and trans-epidemal water loss are strongly correlated with BMI and encapsulated by the BMI metric in this work. We start by quantifying the range of reflectances of human skin. The Monte-Carlo model of skin reflectance follows the path of individual randomly scattered photons and how they are absorbed in different layers of material [15]. In 2017, researchers used a spectrophotometer to collect 400 reflectance data points for green, red, and IR light across a range of human skin tones [16]. The frequency of reflectance values for those 400 measurements shown in *Figure 12.*

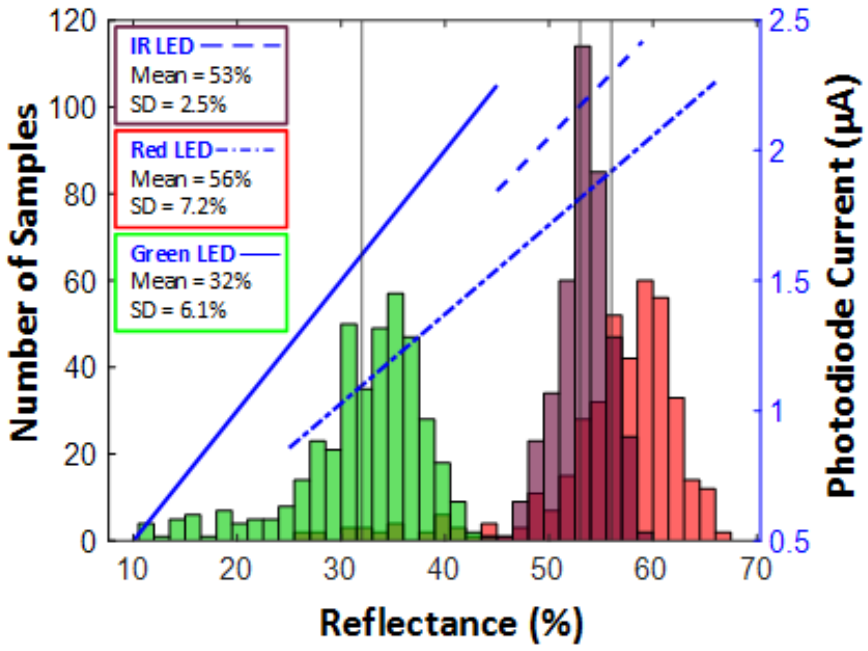

Figure 12: *Impact of skin reflectance on photodiode current with frequency of skin reflectance values for each LED color.*

This data set did not state that it included subjects with tattoos. Because the ink from a tattoo sits at the same layer of the skin as melanin, it affects the reflectance of human skin in a similar manner [28]. An informal test found that red and black solid tattoos had the greatest effect on PPG sensing [24] The effect of tattoos on PPG sensing has not been quantified, so we will view tattoos as less reflective than the least reflective natural skin phototype in this model. Next, we discuss the effects of skin tone and BMI on the AC/DC ratio of a PPG signal. AC/DC ratio shows how the PPG signal degrades with respect to BMI and skin tone. If the AC/DC ratio is too low, the PPG output will not contain a usable waveform. [16] shows the AC/DC ratio for different skin type, measurement locations (wrist and fingertip) and LED color. Of the physiological effects high BMI has, dermal thickness has the largest effect on the PPG signal causing up to a 41.4% decrease in the AC/DC ratio [15]. Boonya - Ananta et al. report the AC/DC ratio of a modeled PPG signal for 5 different BMIs. 8.1% for 25 BMI, 6.6% for 35 BMI, 6.25% for 37 BMI, 5.9% for 40 BMI and 4.6% for 45 BMI. Linear regression was then used to find the AC/DC ratio for 20 to

45 BMI. The effect of skin tone and BMI on the AC to DC ratio have been discussed and quantified individually but these factors can not be looked at independently. This model uses a novel “superscore” that takes into account the reflectance caused by melanin in the skin as well as AC signal strength and degradation as a factor of both skin tone and BMI. We use the reflectance and change in AC/DC ratio to determine the resulting light reflected to the photodiode in the PPG sensor in the next section. It is important to note that mechanical properties such as the distance between the user’s skin and the sensor also affect the amount of light reflected. This portion of the model focuses specifically on the physiological factors, but the potential effects of these mechanical properties are discussed further in the following results section.

4.3.2 PPG Sensor Model

The sensor model is based on the SFH7060 PPG sensor from Osram, which includes a green, red and IR LED for PPG sensing [26]. In order to model the AC component of the PPG signal, we must first determine the total current from the photodiode and its relationship to the LED current. TI refers to this value as the current transfer ratio (CTR) and reports a CTR of .025 μA/mA. This was used to find I_{PDmax} as shown in (9). For the custom system, this value was determined experimentally by measuring I_{DC} on a group of users while applying 2.74 V, 1.8 V, and 1.2 V supply voltages to the green, red, and IR LEDs inside the PPG sensor. The measured average conversion factor across users and LED colors is 0.00162x. Then this conversion factor value was related to the average reflectance value (32% for green, 56% for red and 53% for IR) as shown in *Figure 11* to find the maximum photodiode current (I_{PDmax}) as shown in (10) that could be used to find the I_{DC} for all skin reflectance.This value is then multiplied by the AC/DC ratio given in [26, 15]. This AC/DC ratio also varied based on skin reflectance, measurement location (wrist or fingertip) and LED color. The photodiode current produced with the green, red, and IR LEDs have comparable AC components but the red and IR LEDs have a DC component almost 10x higher than green, which requires higher AFE dynamic range. This is one reason that green is used more widely in commercial devices and is the LED color considered in model

tests and validation for the remainder of this paper. The AC/DC and reflectance values are multiplied by the maximum expected photodiode current to determine the ac current in the photodiode (11). This will later be used to determine SNR. The power of the sensor is shown in (12) where t accounts for the startup and settling time of the AFE. The power of the PPG sensor is also affected by the sampling frequency (f_s) and LED current I_{LED}.

$$I_{PDmaxT1} = CTR * I_{LED} \frac{1}{mean\,reflectance}. \quad (9)$$

$$I_{PDmaxULP} = 0.00162 * I_{LED} \frac{1}{mean\,reflectance}. \quad (10)$$

$$i_{ac} = I_{PDmax} * reflectance * \frac{AC}{DC}. \quad (11)$$

$$P_{LED} = V_{LED} I_{LED} * t * f_s. \quad (12)$$

4.3.3 Custom AFE Model

This portion of the model looks at the noise and power consumption of the custom ULP AFE. This AFE is composed of a (TIA), programmable gain amplifier (PGA), low pass filter (LPF) and an analog-to- digital converter (ADC) [12]. The power is a function of constant voltage (V_{AFE}) and total current (I_{AFE}) which scales with the bias current (I_b) of the system, the sampling frequency (f_s) also referred to as the pulse repetition frequency (PRF), and the associated timing (t), shown in (13). The startup and settling time are also important metrics that contribute to the overall power of the AFE and PPG sensor and scale with I_b.The scaling factor between I_{AFE} and I_b is determined by the TIA architecture and is obtained through SPICE simulations. It is important to note that the power consumption of the TIA is orders of magnitude larger than the power of the components in the rest of the AFE so this model excludes the other components in the power calculation.

The current noise, (i_{rms}), is necessary to later calculate SNR, a key metric in this model. i_{rms} is a function of the voltage (V_{rms}) and the TIA gain. The noise at the output of the TIA (V_{rms}) changes slightly across (I_b) and the transimpedance gain drops as I_b increases. Therefore, the total input-referred current noise (i_{rms}) increases as I_b increases. The current noise across the full range of I_b was determined through simulation. i_{rms} is used to calculate SNR in a later section.

$$P_{AFE} = V_{AFE} * I_{AFE} * f_s * t. \quad (13)$$

4.3.4 TI AFE Model

The second part of this model is based on the TI AFE4404 Ultra-small, Integrated AFE [27]. This AFE is composed of a TIA, noise filter and an ADC with a fully integrated LED driver. This AFE has an LED current range of 0 to 50 mA and 10kΩ to 2MΩ gain. This model looks at 1.6, 3.8 and 4.8 mA and 10kΩ, 25kΩ, 50kΩ and 100kΩ TIA gain. The I_{LED} values were selected because they were the lowest available for the system and would allow for the closest comparison to the ULP systems. The gain values selected made it easy to acquire a signal for every participant during the on-body measurements. From the data sheet, the i_{rms} was determined to be 850pA for 10kΩ gain, 325pA for 25kΩ gain, 175pA for 50kΩ gain and 90pA for 100kΩ gain. The power of the TIAFE4404 is the power consumed by the LED, Tx and Rx stages. The receiver operates at 2V and TI provides the Rx current consumption for different pulse repetition frequencies. This model uses a 100 Hz pulse repetition frequency (PRF) which results in a 250μA receiver current. The equations below model the power for the custom AFE. The transmitter operates at 3 V and consumes 5 μA independent of the LED.

$$P_{Rx} = 2V * I_{rx}. \quad (14)$$

$$P_{Tx} = 3V * I_{rx} + I_{LED}. \quad (15)$$

$$P_{TIAFE} = P_{Rx} + P_{Tx}. \quad (16)$$

4.3.5 System Level Metrics

The two metrics that affect design level decisions in PPG sensors for wearable health are total system power given by (17) and SNR shown in (18) With constant voltage, AFE power is dependent on I_b, and sampling frequency(f_s). PPG sensor power is dependent on I_{LED}, I_b, and f_s. SNR is determined by i_{rms} given in (19), as well as the ac component of the photodiode current i_{ac} which, in turn, is dependent on human skin reflectance and LED color. Therefore, design knobs such as the AFE biasing current I_b, and the LED current I_{LED} are swept to examine how they will affect the system power and SNR with different human skin reflectance, with results shown in the next section. In an effort to focus on the effect of physiological factors, the sampling frequency, also referred to as the pulse repetition frequency, is held constant at 30 Hz.

$$P_{total} = P_{AFE} + P_{LED}. \tag{17}$$

$$SNR = 20log_{10}\frac{i_{ac}}{\sqrt{i_{rms}^2}}. \tag{18}$$

$$i_{rms} = \frac{v_{rms}}{gain}. \tag{19}$$

4.4 Modeling Results

The first focus is on the power of the system with the custom ULP AFE. *Figure 13* shows the relationship between bias current I_b, startup and settling time and the total AFE power. In this system, the AFE is duty-cycled with the LED but the AFE requires some settling and startup time before a signal can be acquired. As I_b is reduced, the required startup and settling time must be increased. This startup and settling time is represented as t(us) in *Figure 13.* As can be observed in the figure, the AFE power is orders of magnitude lower than the power consumed by the LED in the PPG sensor. As a result, the total system power closely follows the power consumption of the LED. Because the LED is the dominating factor in power, designers should aim to choose the lowest LED power possible and adjust other design knobs to compensate. The AFE and LED power trends are also consistent across I_{LED} values. *Figure 13* also demonstrates that the lowest I_b value does not result in the lowest power value. The power of the TI AFE sensing system is also dependent on the LED current. The pulse repetition

frequency affects the power but on a much smaller scale, so we focus on the power as a result of the LED current. The TI AFE power was found to be 500µW for the LED and PRF discussed.

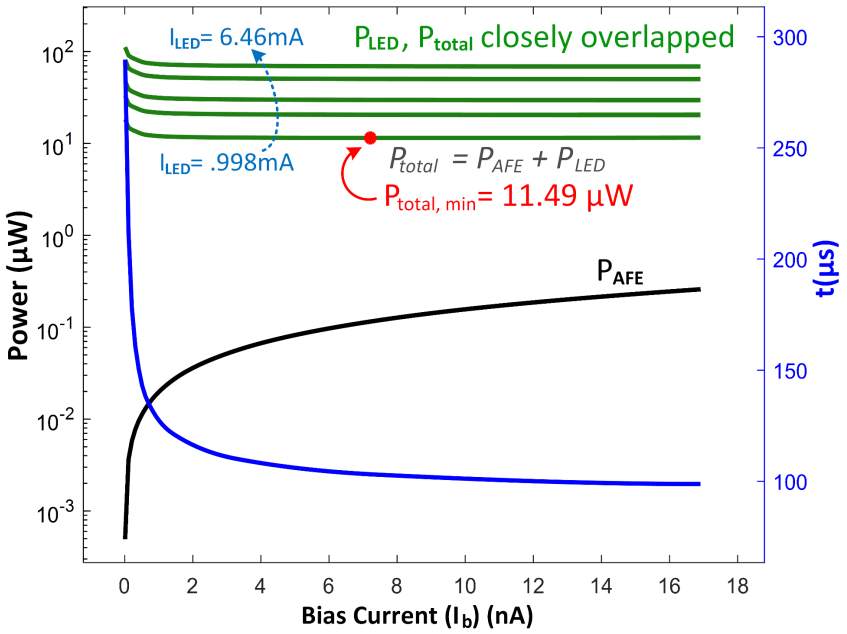

Figure 13: *The relationship between the bias current Ib, resulting required startup and settling time (t) and the total AFE power. These metrics are shown alongside the LED power which closely matches the total system power. The minimum power for the total system is 11.49µW.*

Figure 14 shows the SNR and power tradeoff for the custom ultra low power AFE for the most and least reflective skin phototypes at “normal” and “obese” BMIs, (20, 35 and 45). Every skin type/BMI combination can reach the 60-70 dB SNR range using this system which is acceptable for SpO_2 sensing using PPG. It shows that this is possible at less than 20µW when using the lowest LED current. It also shows a significant increase in SNR as the LED current is increased. Contrary to the claims of Ajmal et al., the skin phototype has a larger effect on SNR than the BMI. We examine the effect of increasing the power on the SNR for the non-obese, most reflective skin and the obese, least reflective skin. For the non-obese, highly reflective case, a 50% increase in power leads to a 5% or 4 dB change in SNR and a 600% increase in power results in a 27% or 16 dB increase in SNR. For the obese, least reflective case, a 50% increase

in power leads to a 3.7% or 9 dB change in SNR and a 600% increase in power leads to a 17% or 16 dB increase in SNR.

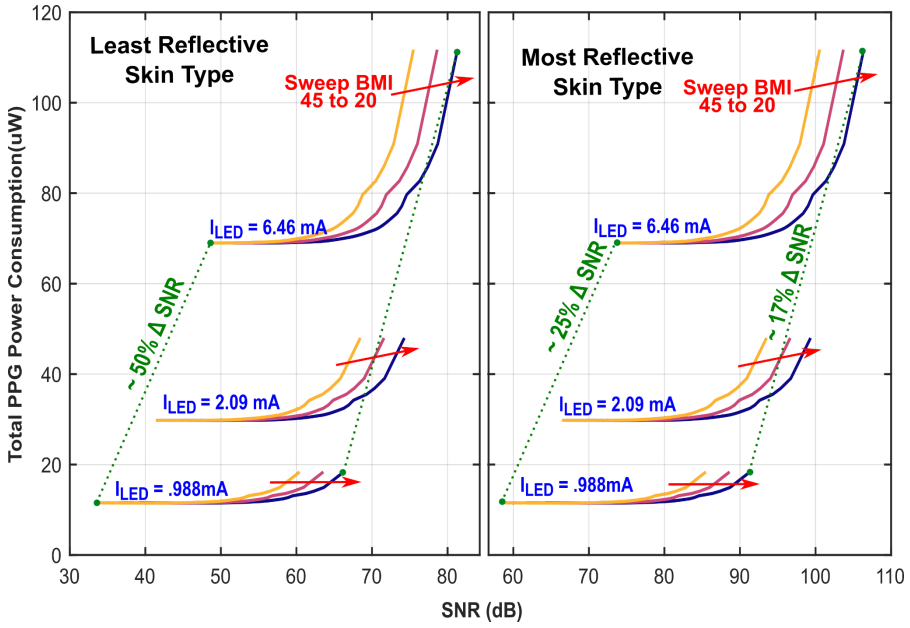

Figure 14: *SNR and power design space tradeoffs for the custom AFE. Three ILED settings are used across BMI and skin tone. The curves on the left side of the figure show the power/SNR tradeoff for subjects with the least reflective skin across 3 BMIs. The right side of the image shows the same tradeoff for the users with the most reflective skin tone.*

Figure 15 shows this same power, SNR trade off for the TI AFE system for the most and least reflective skin phototypes at 20, 30, 35, 40, and 45 BMI. In contrast to the results from the ULP AFE, the increase in SNR when using higher LED current is insignificant. As expected, this model also shows that the skin phototype has a stronger effect on the SNR than the BMI does, and that the higher the BMI is, the more of an effect it has on the SNR. The lower BMIs are grouped more closely together whereas 40 and 45 BMI have a larger decrease in SNR.

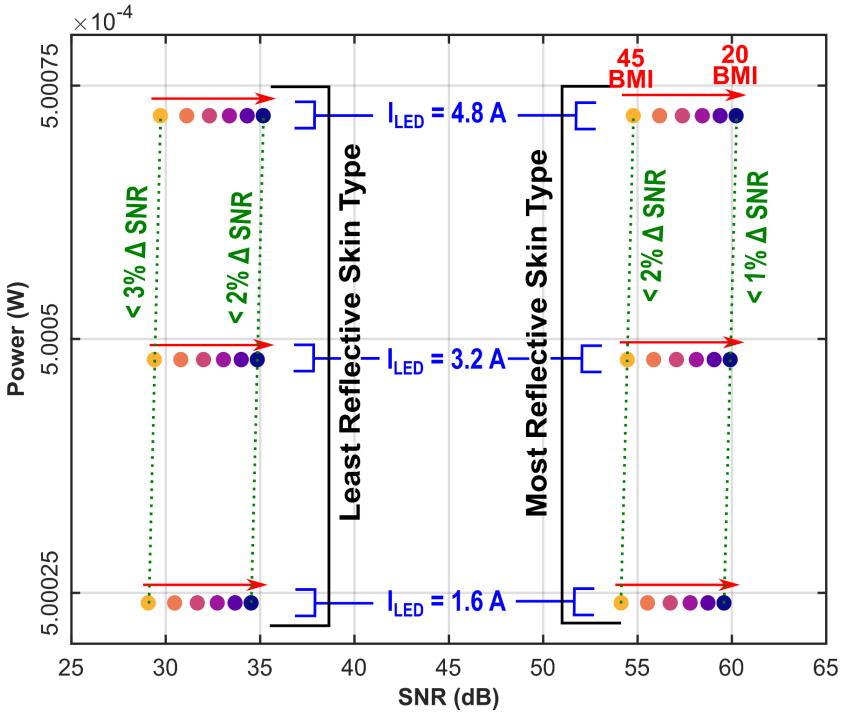

Figure 15: *SNR and power design space tradeoffs for the COTS TI AFE. Three ILED settings are used across BMI and skin tone. Similar to Figure 14, the power/SNR tradeoff is shown for the most and least reflective skin types at different BMIs.*

4.5 On Body Measurements

4.5.1 Methods

After acquiring IRB approval for a human study, we collected fingertip PPG signals, skin type and BMI data from 23 individuals, in accordance with the Helsinki Declaration of 1975 as revised in 2000 to further study the relationship between power, BMI, skin tone and SNR. This study used both the custom AFE discussed above and the TI AFE4404 to collect PPG signals from every participant. The ULP system was tested on a benchtop with the AFE chip in one PCB connected to the SFH7060 sensor on another, smaller PCB. The PPG signal output from the AFE was viewed in an oscilloscope. The TI system was set up on the same benchtop with the main TIAFE4404 board connected to a laptop and the sensor PCB connected to the main TI AFE board. The PPG sensor board used with the TI system had an SFH7050 sensor. This SFH 7050 sensor has fewer emitters than the SFH7060 used with the ULP system but in both cases

only the green emitter was used. The signals were recorded using the software provided by TI. Testing in the same environment allowed the ambient light to be constant. For both the ULP and TI systems the PPG signal data was recorded over a few seconds to show at least five systolic peaks and recorded in a CSV file. In the first portion of the study, researchers used the eight-question Fitzpatrick Skin Type Quiz [29] to determine participant's skin type and a standard BMI chart for participants to self-report their BMI. Participants then sat at the lab bench and held the PCB containing the sensor attached to the ULP system in their left hand and placed their right index finger over the sensor covering both the LED and photodiode completely. Researchers recorded several seconds of data using an oscilloscope at LED voltages 2.6 to 3 mV corresponding to. 234 to 8.5 mA and TIA biasing voltages 130 mV, 112 mV and 70 mV. 130 mV bias corresponds to a 5.6MΩ gain, 112 mV corresponds to a 4.7MΩ gain and 70 mV corresponds to a 2.5MΩ gain. These points were selected to cover a range of settings across power from 15-225 μW of power consumption. Participants then switched to the TI system. They again held the sensor PCB in their left hand and placed their right index finger completely covering the LED and photodiode of the sensor. Researchers recorded several seconds of data at 10kΩ, 25kΩ, 50kΩ, and 100kΩ gain and 1.6 A, 3.2 A, 4.8 A LED. These values allow for the most direct comparison between the custom and TI measured results. The purpose of these measurements was to compare the data collected from the ULP system to the UPL system model and the data from the TI system to the TI system model. In an effort to control the ambient conditions not accounted for in the model, participants were seated in the same position for every study and the same sensors and AFEs were used in every study. The recorded signals were processed in MATLAB to determine the ac amplitude and calculate the SNR as discussed in the modeling section.

4.5.2 Results

The results from the on-body measurements are reported in this section to compare the SNR of the signal obtained across different physiological factors. In this section, SNR is examined across skin tone without considering BMI, BMI without considering skin tone and when

considering SNR and BMI together. For the combined skin tone/BMI plots, “most ideal” candidate is one with low BMI and highly reflective skin and the “least ideal” is an individual with higher BMI and less reflective skin. *Figure 16* shows measured points as well as trend lines for SNR vs the combined skin tone/BMI score at the 4 different gain settings in the TI system. *Figure 17* shows the same for the custom ULP AFE at 3 gain settings. These trends are further examined and compared to the ULP system in *Figure 18.* This figure shows the best-fit relationship between SNR and skin phototype, SNR and BMI and SNR and the combined BMI, SNR score for the custom AFE and the TI system. In every case for the UPL AFE, the lowest gain setting resulted in the highest SNR. This is likely because the increased gain increased the DC component of the signal and the dynamic range was not large enough to handle the AC component. In general the range for the gain of the TI system is smaller than the gain for the ULP system, 10 kΩ - 100 kΩ vs 2.5 MΩ to 5.6 MΩ, but the two systems have a similar dynamic range. The higher gain in the TI system, 100 kΩ, effectively amplifies the AC component of the signal without the amplified DC component overwhelming the AC component or causing the TIA to saturate. In the case of the ULP system, the lower gain, 2.5 MΩ, has the same effect, amplifying the AC signal without saturating the amplifier, but the higher gains, 4.7 MΩ and 5.6 MΩ, provide enough amplification to saturate the amplifier so the ac component of the signal is no longer distinguishable This motivates the need for DCOC.

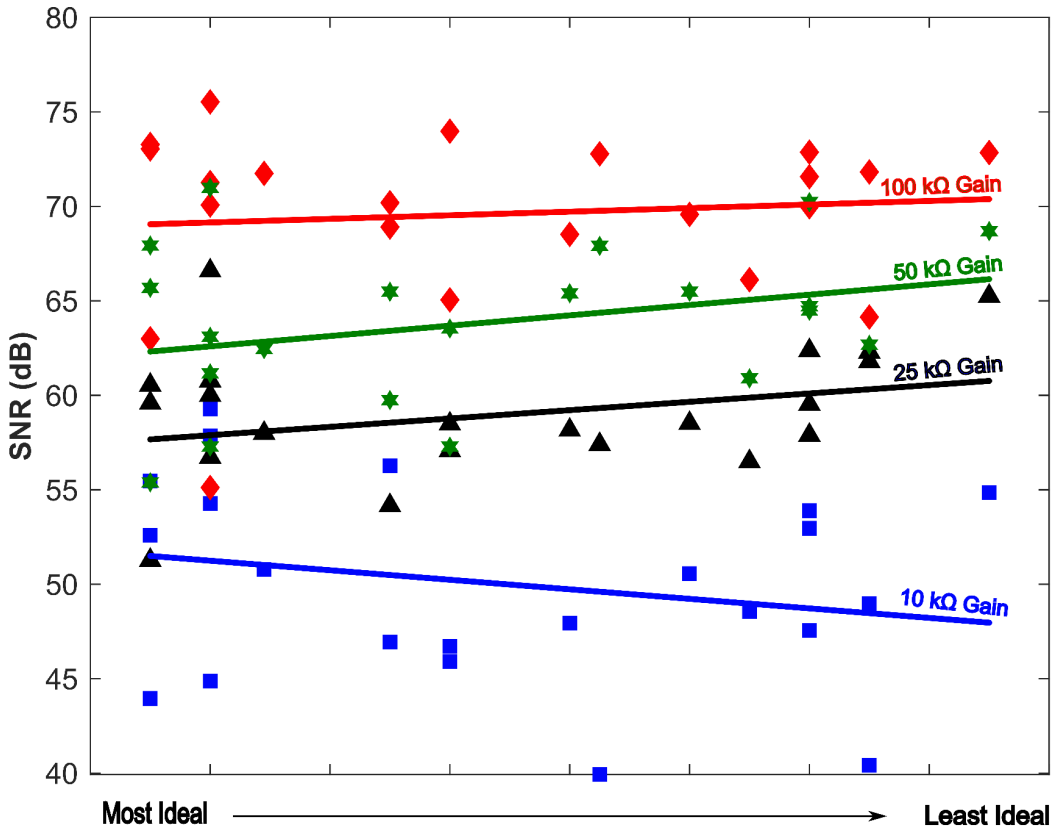

Figure 16: *Measured data points and trend lines from 23 participants using the TI AFE system at 4 different gain settings. "Most Ideal" refers to candidates with the most reflective skin tone and lowest BMI which should result in the largest AC component of the photodiode current. "Least Ideal" refers to the participants with the least reflective skin tone and the highest BMI.*

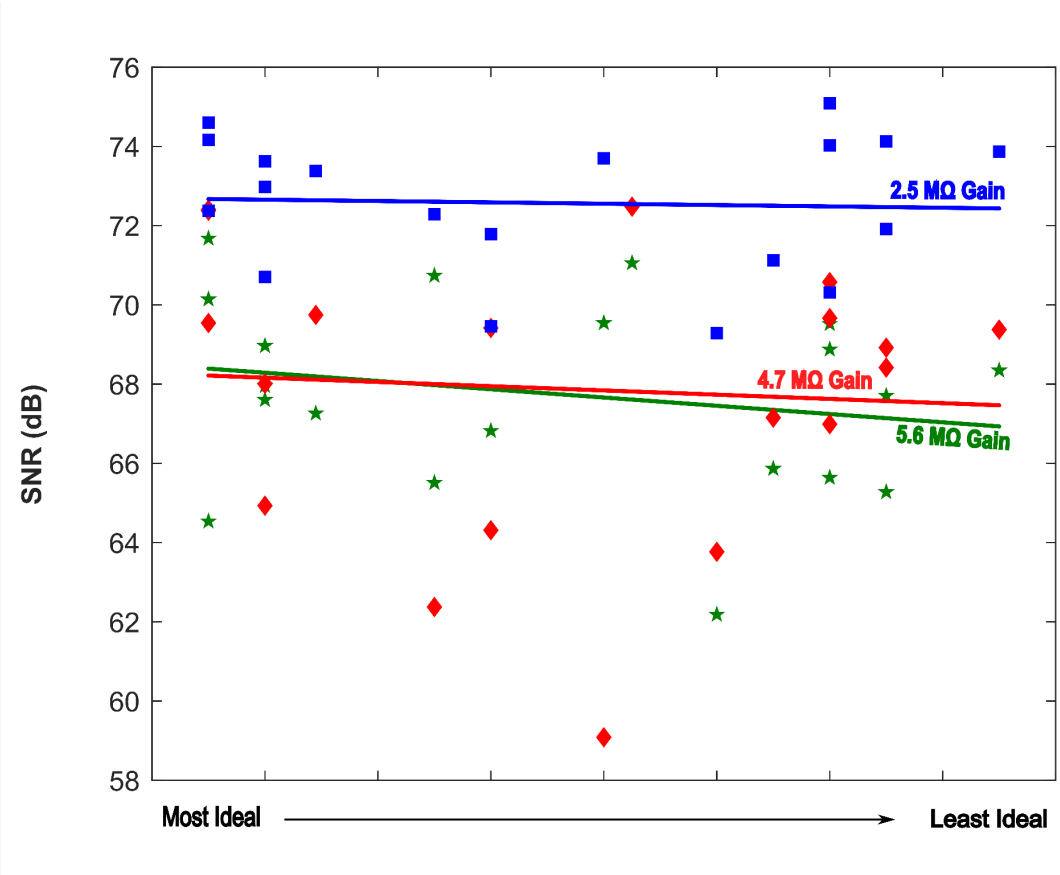

Figure 17: *Measured data points and trend lines from 23 participants using the custom ULP system at 3 different gain settings.*

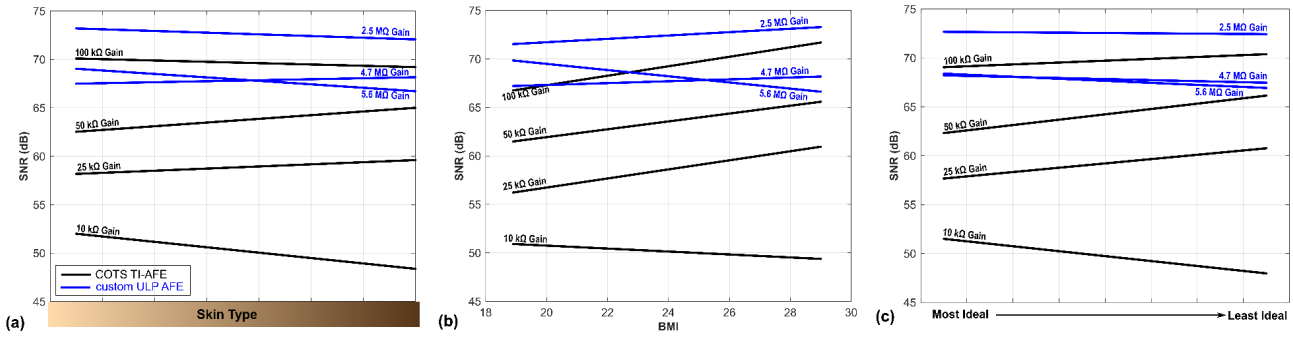

Figure 18:*Trends in measured results from 23 participants showing the relationship between SNR of the measured PPG signal and physiological factors. Data was collected using the commercial TI AFE system at 4 gain settings shown in black and the custom AFE system at 3 different gain settings shown in blue. (a) SNR vs skin phototype, (b) SNR vs BMI, and (c) SNR vs the physiological superscore.*

Another interesting trend arises when looking at the individual skin tone and BMI charts vs. the chart that combines these into a superscore. It is expected that SNR will decrease as skin becomes less reflective or BMI increases but this is not the case at every gain setting when SNR is plotted against skin tone and BMI separately. This is the case for every gain setting when we examine SNR vs the superscore. For the TI system the highest gain, 100 kΩ, yielded the highest SNR. The increased gain effectively increased the AC component of the signal without overwhelming the system with the resulting increase in the DC component. The expected trend discussed above is only shown at the 10 k gain setting. The fact that the high gain effectively increases the SNR and reduces the impact of the skin phototype and BMI on the SNR indicates that there is a way to balance gain, LED current and dynamic range to make system metrics more consistent for all users. *Figure 19* shows the PPG waveform after it was processed using a low pass filter. The waveforms in this figure have SNR values of 58 dB, 62 dB, and 64 dB. These preliminary results demonstrate that it is possible to acquire a strong PPG signal from the fingertip of a subject at ultra-low power.

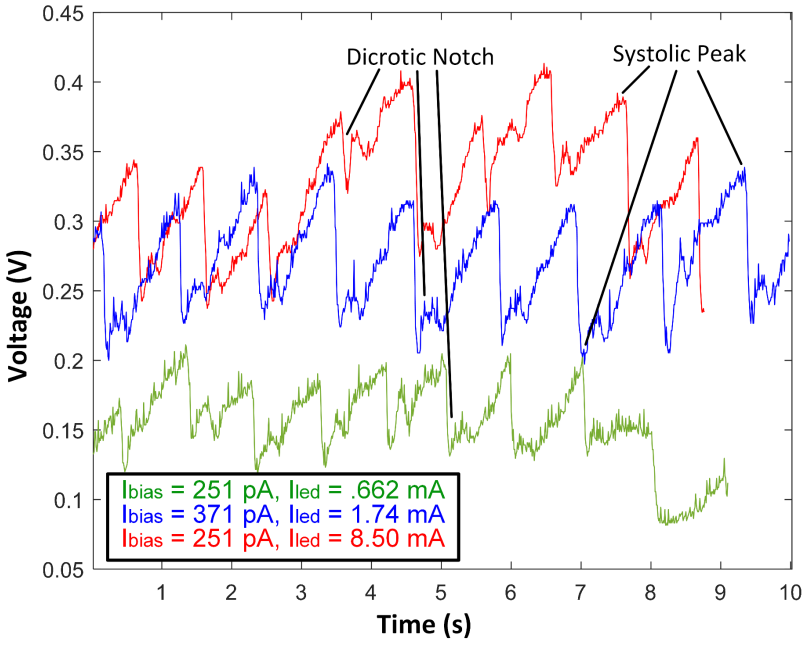

Figure 19: *PPG waveforms measured using the custom ULP AFE and the SFH7060 PPG sensor from Oshram.*

4.6 Discussion of Results and Conclusions

Two main challenges occurred during on-body measurements. The first was the lack of range in skin tone and BMI of the participants. There were no obese or underweight individuals and the skin types represented were not representative of the population in the US. In a study [29], 18.1% of people had skin type 3, 22.2% had skin type 4 and 25% had skin type 5. In this study, 50% were type 3, 45% were type 4 and 5% were type 5. Skin types 1, 2 and 6 were not represented in this study. The other main challenge was the lack of a clear PPG signal on some participants and the effect of pressure on the measurements and the inability to get a signal for some participants. Most participants applied light pressure to get a signal at setting and could hold that same pressure during all measurements. Other participants saturated the amplifier with very little pressure while others could not get enough reflectance even with large amounts of pressure applied. The ability to measure this pressure would allow for a more controlled study. This was not a problem when using the TI system. All participants could apply the same pressure and get a clear signal. The ambient light in the lab where the tests was conducted was constant overhead light so there should be no variation in the ambient light but it is difficult to know how much of the photodiode current is a result of the ambient light. Another factor that affects PPG sensing is the measurement location. This work focuses on measurements at the fingertip, but measurements taken at the chest or wrist would result in an even lower AC/DC ratio [30]. This would require a larger dynamic range which may affect the power of the PPG system.

The main comparison of the modeled results and the measured results focuses on the achievable SNR for each user. For the custom AFE, the model showed a possible range of 30 dB for each individual depending on the gain settings and LED current and the measured results showed a range closer to 6 dB. The range of SNR in the measured results spans 66 dB to 73 dB. This is in the SNR range identified in the model as being achievable for every user regardless of skin phototype or BMI. It is important to recall that the sample size for the measured results are limited, so despite remaining in the achievable range, the modeled results indicate that further outlying samples would not. This is one of the major points that emphasizes

the importance of modeling because the collection of data will always be limited by the sample size. The custom AFE model clearly shows that skin type rather than BMI has the most effect on the achievable SNR, which was determined by the impact on the AC/DC ratio. It was found that this is only the case at 2 gain settings in the measured results, indicating that there may be a more complicated relationship between gain and the AC/DC ratio resulting from skin type and BMI than is captured in the model. Benchmarking *Table I* emphasizes the importance of understanding the limitations in models, and how modeled results compare to existing deployed systems.

Table I: Comparison of Modeled and Measured Results to Previous Work

	[12]	**[13]**	**[14]**	**[19]**	**[29]**	**[30]**	*This Work Modeled*	*This Work Measured*
Supply Voltage	3.3V	1.2/3.3V	1.2V	1.5V	0.5V	5V	0.6V	0.6V
AFE Power Consumption	29.1μW	89μW	54μW	69μW	3μW	400μW	115nW	14.8nW
LED Power Consumption	90-480μW	196μW	121μW	102μW	1.103mW	4.8mW	11.38μW	5.085μW
Total Power Consumption	38.1-489μW	196μW	12μW	102μW	1.103mW	4.8mW	11.49μW	5.1μW

As observed, the model predicts a total power consumption of 5.1μW where the measured system consumes 11.49μW. This discrepancy can be attributed to the differences in modeling assumptions and physical implementation, but the model provides a good target range for designers. The distance between the user's skin and LED varies depending on the pressure

applied. This is true in a real use scenario and difficult to control. Though we intend to examine the relationship between the physiological factors, skin tone and BMI, it should be noted that these results are also dependent on the distance between the user and the LED which was not quantified in this study. Each user was in contact with the LED and photodiode but their finger width and pressure can cause small variations in this distance. The practical considerations discussed in the previous section likely contribute to the discrepancies between the modeled and measured results. In order to commercialize ULP PPG sensing devices, researchers would need to conduct extensive studies around the effect of packaging, pressure on the device, ambient light and other effects not captured in the model. The complex nature of human skin reflectance and vasculature makes it difficult to capture in a model designed to examine more straightforward tradeoffs. Extensive models that incorporate human physiological and optical models could come closer to matching measured results and be a valuable tool for examining the accuracy of these devices for a diverse population before starting expensive and time-consuming on-body testing and trials.

This modeling effort The main comparison of the modeled results and the measured results focuses on the achievable SNR for each user. For the custom AFE, the model showed a possible range of 30 dB for each individual depending on the gain settings and LED current and the measured results showed a range closer to 6 dB. The range of SNR in the measured results spans 66 dB to 73 dB. This is in the SNR range identified in the model as being achievable for every user regardless of skin phototype or BMI. It is important to recall that the sample size for the measured results are limited, so despite remaining in the achievable range, the modeled results indicate that further outlying samples would not. This is one of the major points that emphasizes the importance of modeling because the collection of data will always be limited by the sample size. The custom AFE model clearly shows that skin type rather than BMI has the most effect on the achievable SNR, which was determined by the impact on the AC/DC ratio. It was found that this is only the case at 2 gain settings in the measured results, indicating that there may be a more complicated relationship between gain and the AC/DC ratio resulting from skin type and BMI than is captured in the model. Benchmarking Table I emphasizes the

importance of understanding the limitations in models, and how modeled results compare to existing deployed systems. As observed, the model predicts a total power consumption of 5.1μW where the measured system consumes 11.49μW. This discrepancy can be attributed to the differences in modeling assumptions and physical implementation, but the model provides a good target range for designers. The distance between the user's skin and LED varies depending on the pressure applied. This is true in a real use scenario and difficult to control. Though we intend to examine the relationship between the physiological factors, skin tone and BMI, it should be noted that these results are also dependent on the distance between the user and the LED which was not quantified in this study. Each user was in contact with the LED and photodiode but their finger width and pressure can cause small variations in this distance. The practical considerations discussed in the previous section likely contribute to the discrepancies between the modeled and measured results. In order to commercialize ULP PPG sensing devices, researchers would need to conduct extensive studies around the effect of packaging, pressure on the device, ambient light and other effects not captured in the model. The complex nature of human skin reflectance and vasculature makes it difficult to capture in a model designed to examine more straightforward tradeoffs. Extensive models that incorporate human physiological and optical models could come closer to matching measured results and be a valuable tool for examining the accuracy of these devices for a diverse population before starting expensive and time-consuming on-body testing and trials.

5. Conclusion

The IoT is an ever growing technological revolution that is a powerful system but has also created many new problems for designers to solve. The goal of this work is to highlight some of the capabilities of modeling with respect to self-powered systems, and to also illustrate the need for modeling to be further developed to aid in system design. The scale and impact of IoT devices are largely limited by the lifetime or longevity of the systems in their respective environments. From a systems perspective, modeling can aid in the realization of the design space that restricts a designer's boundaries by addressing individual components' contributions

to overall system power. Further, test modes and models can be used with statistical representations of environments to determine the functionality of a system when it is being supported solely by the environment. This is useful to help maximize the reliability and availability of deployed sensor nodes. From a sensing perspective, this work presents a three-part model to encapsulate the impact of physiological factors on ULP sensing and its accuracy. Modeling is an extremely powerful tool to aid designers in the exploration of the boundaries of current technology. When customized to specific applications, models can lend powerful insight to the design knobs that can and need to be explored for optimal solutions.

References

[1] D. Dondi, A. Bertacchini, D. Brunelli, L. Larcher and L. Benini, "Modeling and Optimization of a Solar Energy Harvester System for Self-Powered Wireless Sensor Networks," in *IEEE Transactions on Industrial Electronics*, vol. 55, no. 7, pp. 2759-2766, July 2008, doi: 10.1109/TIE.2008.924449.

[2] A. Boulis, “Castalia: Revealing pitfalls in designing distributed algorithms in wsn,” in Proceedings of the 5th International Conference on Embedded Networked Sensor Systems, ser. SenSys ’07. New York, NY, USA: Association for Computing Machinery, 2007, p. 407–408. [Online]. Available: https://doi.org/10.1145/1322263.1322318.

[3] D. Benedetti, C. Petrioli, and D. Spenza, “Greencastalia: An energy-harvesting-enabled framework for the castalia simulator,” in Proceedings of the 1st International Workshop on Energy Neutral Sensing Systems, ser. ENSSys ’13. New York, NY, USA: Association for Computing Machinery, 2013. [Online]. Available: https://doi.org/10.1145/2534208.2534215.

[4] J. Eriksson, F. Osterlind, N. Finne, N. Tsiftes, A. Dunkels, T. Voigt, R. Sauter, and ¨ P. J. Marron, “Cooja/mspsim: Interoperability testing for wireless sensor networks,” ´ in Proceedings of the 2nd International Conference on Simulation Tools and Techniques, ser. Simutools ’09. Brussels, BEL: ICST (Institute for Computer Sciences, Social-Informatics and Telecommunications Engineering), 2009. [Online]. Available: https://doi.org/10.4108/ICST.SIMUTOOLS2009.5637

[5] F. Osterlind, A. Dunkels, J. Eriksson, N. Finne, and T. Voigt, “Cross-level sensor network simulation with cooja,” in Proceedings. 2006 31st IEEE Conference on Local Computer Networks, 2006, pp. 641–648.

[6] M. Gorlatova, A. Wallwater, and G. Zussman, Networking Ultra Low Power Energy Harvesting Devices: Measurements and Algorithms, in Proc. IEEE Computer Communications Conference (IEEE INFOCOM'11), Apr. 2011.

[7] Sargolzaeiaval, Y., Ramesh, V. P., & Ozturk, M. C. (2022). A comprehensive analytical model for thermoelectric body heat harvesting incorporating the impact of human metabolism and physical activity. APPLIED ENERGY, 324. https://doi.org/10.1016/j.apenergy.2022.119738

[8] Bishop, Henry. Digital Baseband Techniques and System Modeling Considerations for Low-Power Duty-Cycled Wake-up Receivers. University of Virginia, Electrical Engineering - School of Engineering and Applied Science, PHD (Doctor of Philosophy), 2021, 2021, doi.org/10.18130/33cv-8c91.

[9] O. O’Carroll et al., “Remote monitoring of oxygen saturation in individuals with COVID-19 pneumonia,” Eur. Respir. J., vol. 56, no. 2, Aug. 2020, Art. no. 2001492.

[10] M. Hyland, H. Hunter, J. Liu, E. Veety, and D. Vashaee, “Wearable thermoelectric generators for human body heat harvesting,” Appl. Energy, vol. 182, pp. 518–524, Nov. 2016.

[11] K. A. Flynn, N. B. Ownby, P. Wang, and B. H. Calhoun, “Modeling energy-aware photoplethysmography hardware for personalized health care applications across skin phototypes,” in Proc. IEEE Biomed. Circuits Syst. Conf., 2021, pp. 01–06.

[12] H. L. Bishop, P. Wang, and B. H. Calhoun, “Application-driven model of a PPG sensing modality for the informed design of self-powered, wearable healthcare systems,” in Proc. IEEE Int. Symp. Circuits Syst., 2020, pp. 1–5.

[13] F. Yildiz, “Potential ambient Energy-Harvesting sources and techniques,” J. Tech. Stud., vol. 35, no. 1, pp. 40–48, 2009..

[14] P. J. Colvonen, P. N. DeYoung, N.-O. A. Bosompra, and R. L. Owens, “Limiting racial disparities and bias for wearable devices in health science research,” Sleep, vol. 43, no. 10, Oct. 2020, Art. no. zsaa159.

[15] T. AjmalA. J. Boonya-Ananta, V. N. R. Du Le, and J. C. Ramella-Roman, “Monte carlo analysis of optical heart rate sensors in commercial wearables: The effect of skin tone and obesity on the photoplethysmography (PPG) signal,” Biomed. Opt. Exp., vol. 12, no. 12, pp. 7445–7457, Dec. 2021.

[16] C. C. Cooksey, D. W. Allen, and B. K. Tsai, “Reference data set of human skin reflectance,” J. Res. Nat. Inst. Stand. Technol., vol. 122, pp. 1–5, Jun. 2017.

[17] A. Fawzy et al., “Racial and ethnic discrepancy in pulse oximetry and delayed identification of treatment eligibility among patients with COVID-19,” JAMA Int. Med., vol. 182, no. 7, pp. 730–738, 2022.

[18] P. E. Bickler, J. R. Feiner, and J. W. Severinghaus, “Effects of skin pigmentation on pulse oximeter accuracy at low saturation,” Anesthesiology, vol. 102, no. 4, pp. 715–719, Apr. 2005.

[19] D.-H. Jang and S. Cho, “A 43.4 μW photoplethysmogram-based heartrate sensor using heart-beat-locked loop,” in Proc. IEEE Int. Solid - State Circuits Conf., 2018, pp. 474–476.

[20] Q. Lin et al., “A 119db dynamic range charge counting light-to-digital converter for wearable PPG/NIRS monitoring applications,” IEEE Trans. Biomed. Circuits Syst., vol. 14, no. 4, pp. 800–810, Aug. 2020.

[21] S. Song et al., “A 769 μW battery-powered single-chip SoC with BLE for multi-modal vital sign monitoring health patches,” IEEE Trans. Biomed. Circuits Syst., vol. 13, no. 6, pp. 1506–1517, Dec. 2019.

[22] A. S. Nunez, “A physical model of human skin and its application for search and rescue,” Ph.D. dissertation, Dept. Elect. Comput. Eng., Ohio, OH, USA, 2009.

[23] P. Wang, “Ultra-low power multi-modal sensor interface circuits and systems for personalized physiological monitoring,” Ph.D. Dissertation, Univ. Virginia, 2021.

[24] J. Lee, D.-H. Jang, S. Park, and S. Cho, “A low-power photoplethysmogram-based heart rate sensor using heartbeat locked loop,” IEEE Trans. Biomed. Circuits Syst., vol. 12, no. 6, pp. 1220–1229, Dec. 2018.

[25] A. Sharma et al., “A sub-60- μA multimodal smart biosensing SoC with gt;80-db SNR, 35-μA photoplethysmography signal chain,” IEEE J. SolidState Circuits, vol. 52, no. 4, pp. 1021–1033, Apr. 2017.

[26] Osram Opto Semiconductors, “BioMon sensor datasheet version 1.1,” SFH7060 datasheet, Apr. 2016.

[27] Texas Instruments, “AFE4404 ultra small, integrated AFE for wearable, optical, heart rate monitoring and biosensing,” AFE4404 datasheet, Jun. 2015.

[28] M. Haedersdal, N. Bech-Thomsen, and H. C. Wulf, “Skin reflectanceguided laser selections for treatment of decorative tattoos,” Arch. Dermatol., vol. 132, no. 4, pp. 403–407, Apr. 1996.

[29] S. Y. He, C. E. McCulloch, W. J. Boscardin, M.-M. Chren, E. Linos, and S. T. Arron, “Self-reported pigmentary phenotypes and race are significant but incomplete predictors of fitzpatrick skin phototype in an ethnically diverse population,” J. Amer. Acad. Dermatol., vol. 71, no. 4, pp. 731–737, Oct. 2014.

[30] Q. Lin et al., “28.3 a 28 μW 134db DR 2nd-order noise-shaping slope light-to-digital converter for chest PPG monitoring,” in Proc. IEEE Int. Solid- State Circuits Conf., 2021, pp. 390–392.

[31] D. Castaneda, A. Esparza, M. Ghamari, C. Soltanpur, and H. Nazeran, “A review on wearable photoplethysmography sensors and their potential future applications in health care,” Int. J. Biosens. Bioelectron., vol. 4, no. 4, pp. 195–202, Aug. 2018.

[32] T. Tamura, “Current progress of photoplethysmography and SPO2 for health monitoring,” Biomed. Eng. Lett., vol. 9, no. 1, pp. 21–36, Feb. 2019.

[33] W. Saadeh, S. Z. Aslam, A. Hina, and F. Asghar, “A 0.5v PPG-based heart rate and variability detection system,” in Proc. IEEE Biomed. Circuits Syst. Conf., 2018, pp. 1–4.

[34] M. Tavakoli, L. Turicchia, and R. Sarpeshkar, “An ultra-low-power pulse oximeter implemented with an energy-efficient transimpedance amplifier,” IEEE Trans. Biomed. Circuits Syst., vol. 4, no. 1, pp. 27–38, Feb. 2010.

[35] B. Lin, Z.Ma,M. Atef, L. Ying, and G.Wang, “Low-power high-sensitivity photoplethysmography sensor for wearable health monitoring system,” IEEE Sens. J., vol. 21, no. 14, pp. 16141–16151, Jul. 2021.

[36] L. Zhao and Y. Jia, “Towards a self-powered ECG and PPG sensing wearable device,” in Proc. 43rd Annu. Int. Conf. IEEE Eng. Med. Biol. Soc., 2021, pp. 6791–6794.

[37] B. Bent, B. A. Goldstein, W. A. Kibbe, and J. P. Dunn, “Investigating sources of inaccuracy in wearable optical heart rate sensors,” NPJ Digit. Med., vol. 3, pp. 1–9, Feb. 2020.

[38] S. F. Alamouti, C. Yalcin, J. Jan, J. Ting, A. C. Arias, and R. Muller, “An SpO2 sensor using reconstruction-free sparse sampling for 70% system power reduction,” in Proc. IEEE Int. Solid- State Circuits Conf., 2022, pp. 344–346.